ACS NANO

www.acsnano.org

ARTICLE

Optical Single-Channel Recording via Diffusional Confinement in Membrane Tethers

Madeleine R. Howell and Adam E. Cohen*

Cite This: https://doi.org/10.1021/acsnano.5c07589

Read Online

ACCESS | Metrics & More | Article Recommendations | Supporting Information

ABSTRACT: **Single-channel electrophysiology probes ion channel gating, but how can one probe membrane transport when the single-unit current is undetectable? We pulled membrane tethers from live cells to isolate individual transmembrane proteins. The tether constrained diffusion of the transported substrate to the tether axis, leading to ∼1000-fold enhancement of substrate concentration and observation time compared to planar membranes. Fluorescent reporters inside the tether revealed individual transport events. We imaged unitary Ca^{2+} transport events in tethers containing the low-conductance T-type Ca^{2+} channel $Ca_V3.2$ and compared our results to ensemble electrophysiology and stochastic gating simulations. We detected events corresponding to as little as ∼0.4 fC of transported charge, or only 6−13 free Ca^{2+} ions under typical buffering conditions. Tether-based single-channel recordings are a powerful tool to study dynamics of membrane transport.**

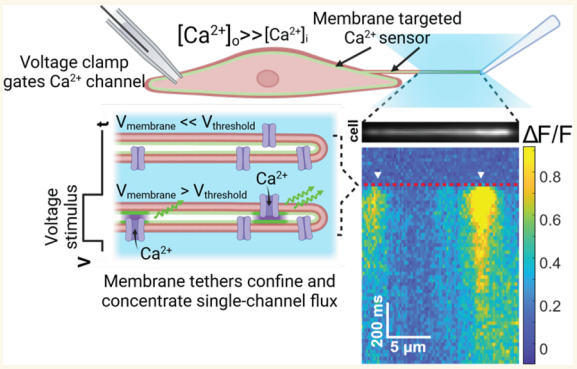

KEYWORDS: *single molecule, membrane transport, fluorescent sensors, signal confinement, live cell imaging*

The plasma membrane of eukaryotic cells is decorated by diverse ion channels, transporters, and membrane-associated enzymes which orchestrate electrical and chemical signaling, osmotic regulation, and aspects of metabolism.[1−3] The transport properties of these proteins are critical to their function. Single-channel electrophysiology[4−7] can reveal molecular mechanisms of ion channel gating and regulation, but many channels and transporters remain inaccessible to this technique because either they are not electrogenic, or the single-unit current is too small (<∼100 fA).[8,9]

Optical recordings of transmembrane flux using fluorescent reporters[10] can also probe single-channel transport. Optical recordings have measured Ca^{2+} flux through single voltage- and ligand-gated channels, using either fluorogenic Ca^{2+} dyes or a genetically encoded Ca^{2+} indicator (GECI) tethered to the channel.[11−18] However, rapid dilution of transported ions into the cytoplasm limits the sensitivity of this approach. Isolation of single transporters in purified nanoscale proteoliposomes achieves single-channel sensitivity by preventing diffusive dilution of transported molecules.[19,20] However, this cell-free approach requires protein purification, loses the native cellular context, and restricts molecular or electrical access to the lumen of the liposomes.

Membrane tethers consist of thin (typically ∼100 nm diameter) tubes of membrane which can be pulled from many cell types in culture.[21] The tether lumen remains in diffusive interchange with the cell body, while the tether membrane restricts diffusion along the two orthogonal axes. Thus, tethers are intermediate between intact cell membrane and purified proteoliposomes: they provide substantial diffusive confinement but retain much of the physiological context and provide molecular and electrical access to the lumen.

Here, we pulled membrane tethers from intact cells and used a fluorescent reporter to record single-molecule gating events within the tether (Figure 1A,B). We recorded single-channel events from $Ca_V3.2$, a low-conductance (<2 pS) and transiently activated voltage gated calcium channel (VGCC),[22,23] using a membrane-targeted genetically encoded calcium indicator (GECI).[24,25] Voltage-clamp in the parent cell controlled the gating of single channels. We related the single-channel gating properties to ensemble $Ca_V3.2$ currents, and used stochastic gating simulations to interpret our results.

Received: May 7, 2025
Revised: June 28, 2025
Accepted: June 30, 2025

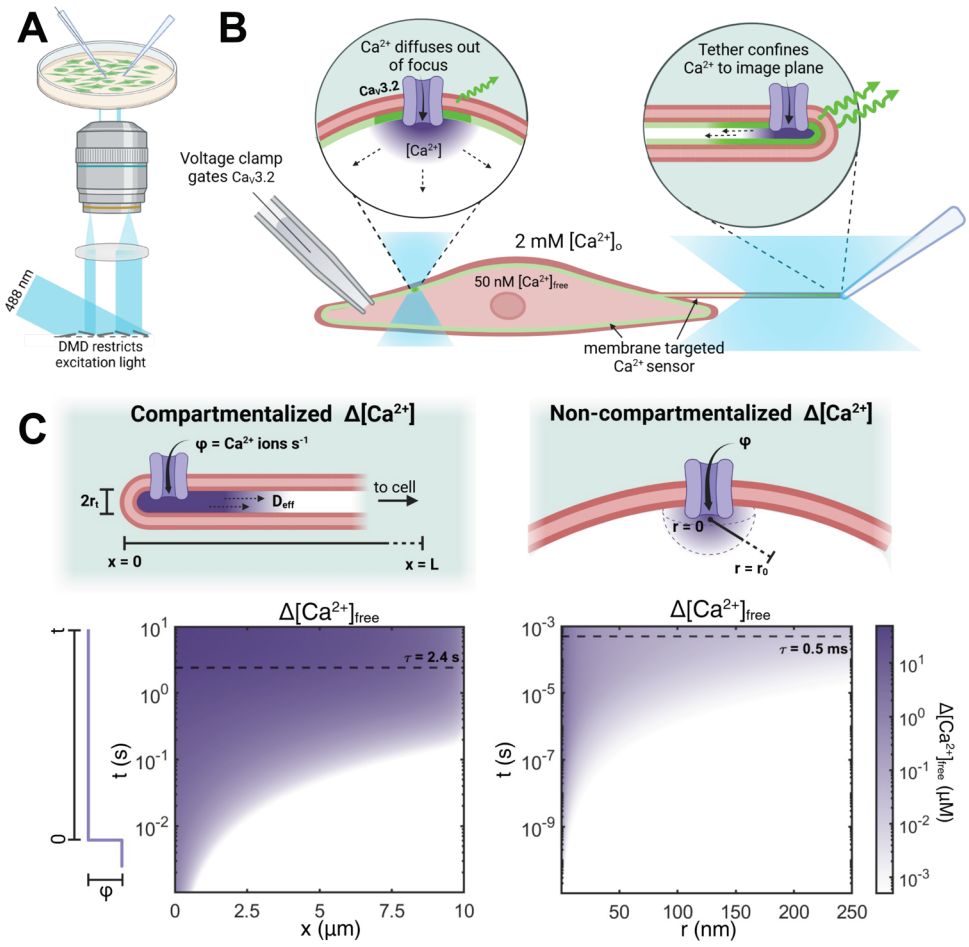

Figure 1. Single-channel recording in membrane tethers. (A) Experimental setup comprising patterned illumination from a digital micromirror device (DMD) and two pipettes controlled by micromanipulators. (B) Schematic of the experiment. A HEK293 cell expressed $Ca_V3.2$ and a membrane-targeted Ca^{2+} indicator. One pipette applied voltage steps to gate the Ca_V channels. A second pipette pulled a membrane tether, which confined the Ca^{2+} influx from single Ca_V gating events. DMD-targeted illumination of the tether minimized background fluorescence and flare from the much brighter cell. (C) Comparison of a $Ca_V3.2$ channel residing in a tether (left) or the cell body (right). Bottom: simulated Ca^{2+} profiles for the depicted geometries, assuming a step opening of the channel at $t = 0$, a transport rate of $\phi = 10^5$ Ca^{2+} ions/s,[23] an effective diffusion coefficient of $D_{eff} = 21$ $\mu m^2/s$,[26−28] and a buffering capacity (buffer-bound Ca^{2+} per free Ca^{2+})[29] of $\kappa = 200$.[27,30] In the tether, the channel is assumed to reside at the distal end. For the channel in the cell body, the Ca^{2+} concentration is averaged over a hemisphere of radius r. Dashed lines indicate the Ca^{2+} residence time in a tether-delimited (left) and diffraction-limited (right) focal volume. See Table S1 for diffusion model parameters.

RESULTS AND DISCUSSION

Theory of Single-Channel Signal Enhancement in Membrane Tethers. We first modeled Ca^{2+} transport for a single channel residing either within a tether or on the cell body membrane. Details of the model are in Note S1 and Table S1. We modeled the tether as a tube of radius r_t and length L, open to the cell body at its proximal end and sealed at its distal end (Figure 1C). Tether radii were $r_t \sim 50$ nm, set by the balance of membrane rigidity and membrane tension[31] (Figure S1), and lengths were $L \sim 10$ μm. We assumed rapid equilibrium of cytoplasmic Ca^{2+} buffers such that free Ca^{2+} flux, ϕ_{free}, scales inversely with buffer capacity, κ_B, following $\phi_{free} = \phi/(1 + \kappa_B)$, where ϕ is the total flux through the channel.[32] The effective Ca^{2+} diffusion coefficient, D_{eff}, is a weighted average of free and buffer-bound Ca^{2+} diffusion coefficients (eq 2 in Note S1).[33] We compared the Ca^{2+} concentration within a membrane-delimited tether volume to the mean Ca^{2+} concentration within a diffraction-limited confocal volume with radius r_0, centered on a channel in the cell body membrane.

If a Ca^{2+} channel opens and stays open at the distal end of the tether, the steady-state free $[Ca^{2+}]$ concentration has maximal increase at the location of the channel:

$$\Delta[Ca^{2+}]_{free} = \frac{\phi L}{D_{eff}\pi r_t^2(1 + \kappa_B)} \quad (1)$$

and a linear decrease down to $\Delta[Ca^{2+}]_{free} = 0$ at the junction with the cell body. The mean residence time of a Ca^{2+} ion in the tether is

$$\tau = \frac{L^2}{2D_{eff}} \quad (2)$$

For a channel opening in the membrane on the cell body, we model the geometry as a planar membrane opening into an infinite half-space. This approximation is valid over distances much smaller than the size of the cell. In this scenario, Ca^{2+} rapidly diffuses into the open half-space (Figure 1C). The steady state increase, $\Delta[Ca^{2+}]_{free}$, decays with distance r from the channel as $1/r$. We modeled the resulting Ca^{2+} domain as

https://doi.org/10.1021/acsnano.5c07589
ACS Nano XXXX, XXX, XXX−XXX

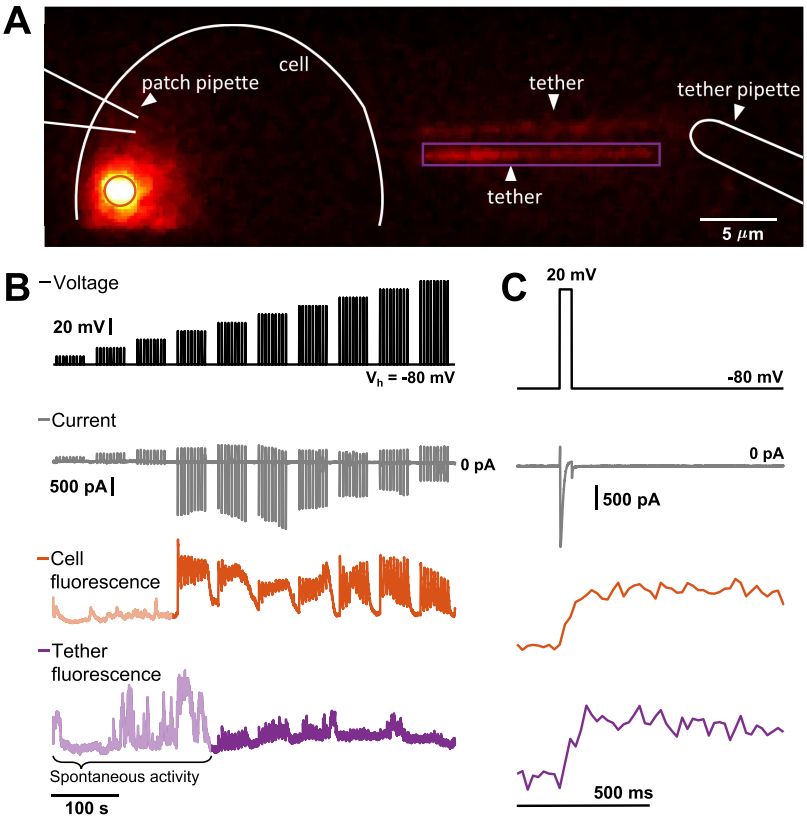

Figure 2. Simultaneous recording of tether and cell body Ca^{2+} dynamics. (A) HEK293 cell expressing $Ca_V3.2$, with localized excitation of a membrane-targeted GECI (GCaMP6s-CAAX) in the cell body (orange circle) and tether (purple rectangle). (B) Concurrent patch-clamp recording of evoked currents (gray) and Ca^{2+}-dependent fluorescence in the cell body (orange) and tether (purple) in response to depolarizing voltage steps (black) of 10−100 mV from a holding potential of −80 mV. Light-shaded regions indicate epochs of spontaneous Ca^{2+} influx, which were excluded from analysis. (C) Magnified view of traces in (B). Trains of nine repeats of 45 ms voltage pulses with a 5 s rest between pulses and a 15 s rest between pulse trains. Current and voltage traces were sampled at 100 kHz. Cell body and tether fluorescence were recorded at 50−200 Hz.

an average of $\Delta[Ca^{2+}]_{free}$ over a diffraction-limited focal volume with radius r_0 centered on the channel, so:

$$\langle \Delta[Ca^{2+}]_{free} \rangle = \frac{3\phi}{4\pi D_{eff} r_0 (1 + \kappa_B)} \quad (3)$$

The mean residence time of a Ca^{2+} ion within this observation volume is

$$\tau = \frac{r_0^2}{6D_{eff}} \quad (4)$$

Our model predicts that a tether of typical dimensions (100 nm diameter, 10 μm long) enhances the steady-state in-focus $\Delta[Ca^{2+}]_{free}$ near the channel by a factor of $r_0 L / r_t^2 \sim 10^3$ compared with diffraction-limited imaging of a Ca^{2+} channel in the membrane of the cell body (Figure 1C and Note S1). The time-resolution with which channel gating converts to changes in $\Delta[Ca^{2+}]_{free}$ is ~10^3-fold slower in the tether than for the channel in the soma membrane. These simple estimates suggest that membrane tethers can render even miniscule steady-state transmembrane flows (ϕ_{free} = 100 s^{-1}, D_{eff} = 200 $\mu m^2/s$) detectable by a fluorescent reporter ($K_D \sim 1$ μM).

Dimensional scaling arguments can also predict the fluorescence decay rates for transiently active channels or pores (Note S1). After a brief influx of Ca^{2+}, in a tether, the local concentration around the influx site decays as $t^{-1/2}$. In a cell, the local concentration decays as $t^{-3/2}$. Thus, tethers provide a longer observation window for detecting brief channel-gating events.

Tether Fluorescence Reports Membrane Ca^{2+} Influx with High Fidelity. We tested whether Ca^{2+} compartmentalization in tethers permitted optical recordings of single-channel gating. In a HEK293 cell line stably expressing doxycycline-inducible $Ca_V3.2$ α1 subunit,[34] we titrated doxycycline to achieve an expression density of ~4 channels/μm^2 (Figure S2 and Methods). We also expressed a membrane-targeted GECI, either lck-jGCaMP8f or GCaMP6s-CAAX.[24,25] A high-efficiency transfection protocol and strong promotor (CMV) drove dense GECI expression, so the GECI molecules were effectively continuous along the tethers (Figure S1 and Methods). We used a patch pipette in whole-cell mode to modulate the membrane voltage and to record ensemble Ca_V currents, and a second pipette to extract tethers. Due to the subdiffraction tether diameter, GECI fluorescence from the tether membrane was far dimmer than from the cell body membrane (Figure S1). To record from both regions, we used a digital micromirror device (DMD) to target 488 nm excitation light onto the tether and onto a small patch of the cell body opposite the junction with the tether (Figure 2A). This illumination strategy minimized the total excitation light, decreasing background autofluorescence and flare from the bright fluorescence of the cell body, which might otherwise have overwhelmed the dim signal from the tether. The tethers were too thin to determine their diameter via

https://doi.org/10.1021/acsnano.5c07589
ACS Nano XXXX, XXX, XXX−XXX

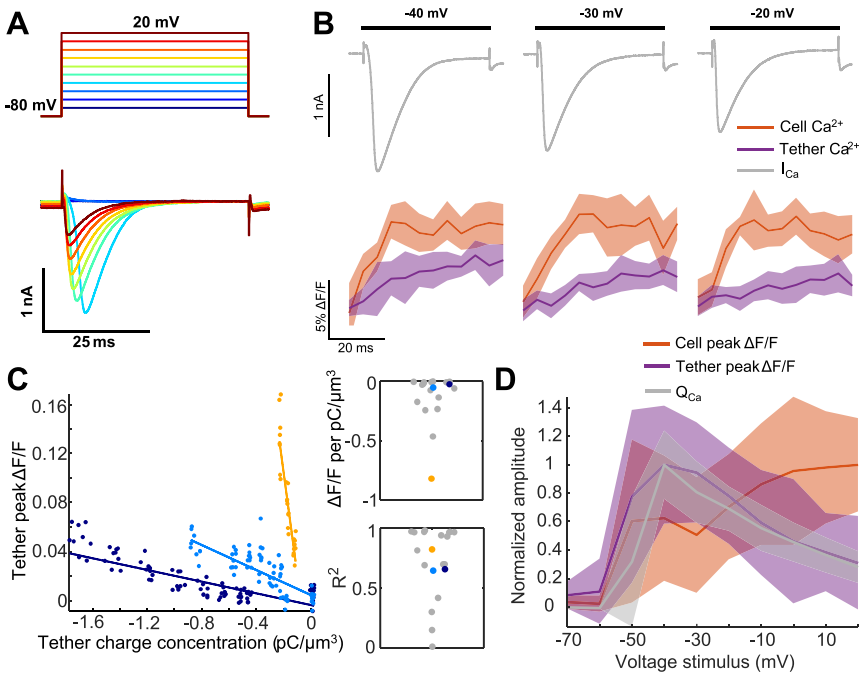

Figure 3. Tether Ca^{2+} signal correlates with whole-cell charge transport. (A) Inward currents (bottom) recorded from a $Ca_V3.2$ expressing HEK293 cell in response to 45 ms depolarizing voltage steps (top). (B) Trial averaged current (top), cell (orange), and tether (purple) lck-jGCaMP8f fluorescence responses to membrane depolarizations. To calculate $(\Delta F/F)^t$, $\Delta F/F$ was first calculated for each position along the tether using the pre-stimulus baseline fluorescence as F and then averaged along the tether length. Data are shown for one cell (n = 9 trials, std. dev. shading). (C) Peak $(\Delta F/F)^t$ amplitude of tether lck-jGCaMP8f fluorescence transients as a function of predicted tether charge concentration, $[Q^t_{Ca}]$, and linear fits. Data and fits are shown for three example tethers. Inset: slope (top) and R^2 (bottom) from linear fits of n = 20 tethers. (D) Voltage dependence of stimulus-evoked charge influx (gray), tether (purple), and cell (orange) peak $\Delta F/F$ amplitudes averaged across n = 25 lck-jGCaMP8f cell-tether pairs. Traces are normalized for each cell-tether pair before averaging and shaded to show std. dev. Tether peak $(\Delta F/F)^t$ and Q_{Ca} were more closely correlated than were cell peak $(\Delta F/F)^C$ and Q_{Ca}.

direct imaging, so we compared GECI fluorescence from the tether and from a patch of the cell membrane of defined area, using the constant GECI fluorescence per-unit-surface-area to determine the ratio of these two areas (Figure S1). These measurements were performed at a holding potential of −80 mV, where Ca_V channel activation is negligible, to ensure the results were not distorted by Ca_V-mediated Ca^{2+} fluxes.

We applied trains of depolarizing voltage pulses from a holding potential of −80 mV, and simultaneously recorded whole-cell currents and GECI-reported Ca^{2+} dynamics in the cell, $(\Delta F/F)^C$, and tether, $(\Delta F/F)^t$ (Figure 2B,C). The camera frame-rate was 50−200 Hz. The voltage steps induced transient inward whole-cell currents which typically returned to zero before the end of the t_V = 45 ms voltage step (Figure 3A). The time constants of $Ca_V3.2$ activation and inactivation decreased for more depolarizing voltages, consistent with prior studies of this channel.[22]

Membrane depolarization evoked Ca^{2+} signals in the cell and tether (Figure 2B,C). Both regions also showed occasional spontaneous Ca^{2+} dynamics (Figure 2B light shading). Epochs with these spontaneous events were omitted from analysis (Methods). An estimate of tether electrotonic length-constant, λ, based on whole-cell membrane conductance and tether geometry, gave $\lambda \sim 110$ μm (membrane resistivity $R_m = 1.5 \times 10^6$ MΩ μm^2; intracellular resistivity $R_i = 3.0$ MΩ μm;[35] radius r = 50 nm), indicating that Ca_V channels throughout the tether experienced membrane voltages similar to the voltage at the cell body. The appearance of voltage-gated Ca^{2+} influx in the tether was consistent with this finding.

For both cell body and tether, the stimulus-evoked GECI fluorescence grew and decayed slowly compared to the patch-clamp recorded currents (Figures 2C and 3B). The upstroke of the GECI fluorescence was much faster (~10 ms) than the recovery (~1.4 s), implying that the peak GECI fluorescence was proportional to the increase in Ca^{2+} concentration due to the voltage step:

$$\max\left(\frac{\Delta F}{F}\right) \propto \frac{1}{\Gamma}\int_0^{t_V} I_{Ca}\,dt \tag{5}$$

where Γ is the volume into which the Ca^{2+} is diluted and I_{Ca} is the absolute value of the inward calcium current.

For each voltage step, we calculated whole-cell charge influx, Q^C_{Ca}, via the integral of the voltage-clamp current recording. We estimated the surface areas of the tether and of the whole cell from the tether geometry (Figure S1) and the whole-cell capacitance, respectively (Figure S2). We initially assumed that channel density was approximately homogeneous across the cell and the tether, so we predicted that the Ca^{2+} flux would be apportioned between the cell (Q^C_{Ca}) and the tether (Q^t_{Ca}) according to their relative surface areas.

We then checked the proportionality across voltage steps between tether Ca^{2+} signal, $(\Delta F/F)^t$, and the predicted tether charge concentration, $[Q^t_{Ca}]$. We observed a clear linear relationship within each tether (Figure 3C and Figure S3), but substantial variation in slope between tethers (Figure 3C inset). The differing slopes likely reflected variation in tether channel density, perhaps due to inhomogeneous channel distributions across the cell leading to variations in the number pulled into each tether. We also observed trial-to-trial

https://doi.org/10.1021/acsnano.5c07589
ACS Nano XXXX, XXX, XXX−XXX

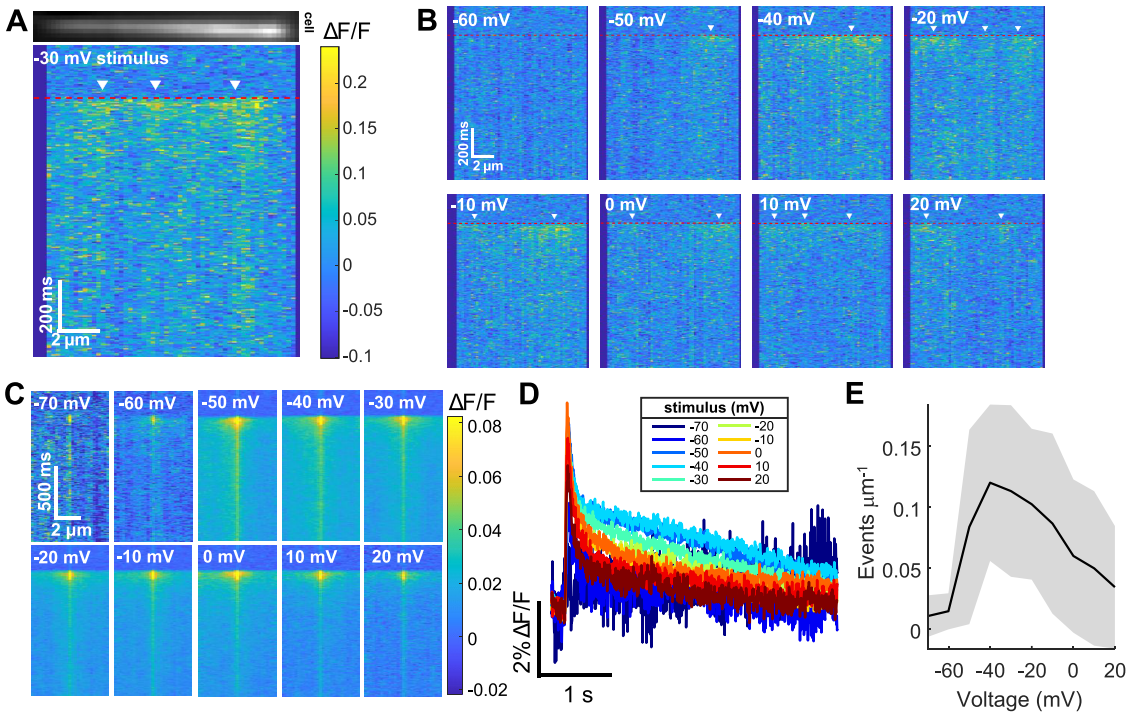

Figure 4. Tether Ca^{2+}signal comprises discrete events. (A) Epifluorescence image of a tether above a kymograph for a 45 ms voltage step from −80 to −30 mV. Red dashed line indicates step onset. White arrowheads indicate discrete Ca^{2+} events. (B) Kymographs of tether Ca^{2+}-dependent fluorescence in response to voltage steps from −80 mV to between −60 and +20 mV. Data are shown for single-trial responses of one tether. (C) Stimulus-triggered average kymographs of spatially isolated tether Ca^{2+} events (8−251 events per voltage, n = 25 tethers, 17 cells). (D) Time-course of events in (C), averaged over space. (E) Linear density of observed Ca^{2+} influx events versus voltage (mean ± s.d., n = 19 tethers).

fluctuations in fluorescence responses within each tether, which we attribute to statistical fluctuations in channel activation within tethers (Figure 3C inset). These fluctuations are expected, considering the small number (∼2−12) of stochastically gating channels per tether (Figure S2).

Unexpectedly, we found that the correlation between $(\Delta F/F)^t$ and Q_{Ca}^C was stronger than the correlation between $(\Delta F/F)^C$ and Q_{Ca}^C (Figure 3D and Figure S3), i.e., whole-cell charge and whole-cell fluorescence-reported Ca^{2+} influx were not well correlated. We speculate that the Ca^{2+} in the cell body may have had additional stochastic uptake and release from internal Ca^{2+} stores (e.g., in mitochondria and endoplasmic reticulum), whereas these organelles were excluded from the tether. Future experiments could explore this issue via pharmacological modulation of internal calcium stores. Since we could not establish a robust relationship between Ca^{2+} influx, Ca^{2+} concentration, and GECI fluorescence in the cell body, we were unable to establish an absolute relation between $(\Delta F/F)^t$ and Q_{Ca}^t. Hence, subsequent measurements focused on analyzing relative changes in $(\Delta F/F)^t$.

Ca^{2+} Indicator Reports Discrete Influx Events. We observed stimulus-triggered Ca^{2+} events which originated from distinct positions along the tether and which fluctuated in number and position between successive voltage steps (Figure 4A,B and Figure S4). We visualized these Ca^{2+} events via kymographs, where fluorescence was displayed as a function of position along the tether and time. We combined smoothing and automated thresholding to identify peaks that were >3 ± 0.9 σ from baseline fluctuations and separated by >0.7 μm (Methods). By comparing recordings taken at the holding potential of −80 mV (when $Ca_V3.2$ channels are expected to be closed) to the recordings during voltage steps, we estimate a false-positive rate of 0.9% (Figure S5).

We calculated stimulus-triggered average spatiotemporal footprints of isolated events (separated by >1.4 μm) (Figure 4C and Figure S4). These footprints captured the rapid depolarization-triggered Ca^{2+} influx and spread. Since the response-time of the Ca^{2+} measurements (∼40 ms to peak) was comparable to the 45 ms duration of the voltage pulse, we could not resolve variations in the onset of Ca^{2+} influx relative to the voltage upstroke.

We observed clear nonexponential decay of the peak Ca^{2+} signal (Figure 4D and Figure S4). The 1-dimensional diffusion kernel for a δ-function impulse of Ca^{2+} is $K(x, t) = \frac{1}{\sqrt{4\pi Dt}}\exp\left(-\frac{x^2}{4Dt}\right)$. Evaluating this expression at x = 0 implies that the peak concentration should decay as $\sim 1/\sqrt{t}$. Figure S6 shows a fit of the fluorescence decay to this simple model. A more detailed model of the fluorescence decay would include dynamic equilibrium of Ca^{2+} with endogenous buffers; the nonlinear and time-dependent relation between Ca^{2+} concentration and GECI fluorescence; overlap of Ca^{2+} from neighboring Ca_V gating events; and slow interchange of Ca^{2+} between the tether and the cell body. Our analysis relied only on the initial peak signal, and so did not depend on these quantities.

We quantified the linear density of gating events in each stimulation epoch (Figure 4E) and observed a peak density of approximately 0.15 μm^{-1}. Assuming statistically independent gating of each channel, the number of gating events is expected to follow Poisson statistics. We estimated that at the maximum activation density of 0.15 μm^{-1}, the probability of two events

https://doi.org/10.1021/acsnano.5c07589
ACS Nano XXXX, XXX, XXX−XXX

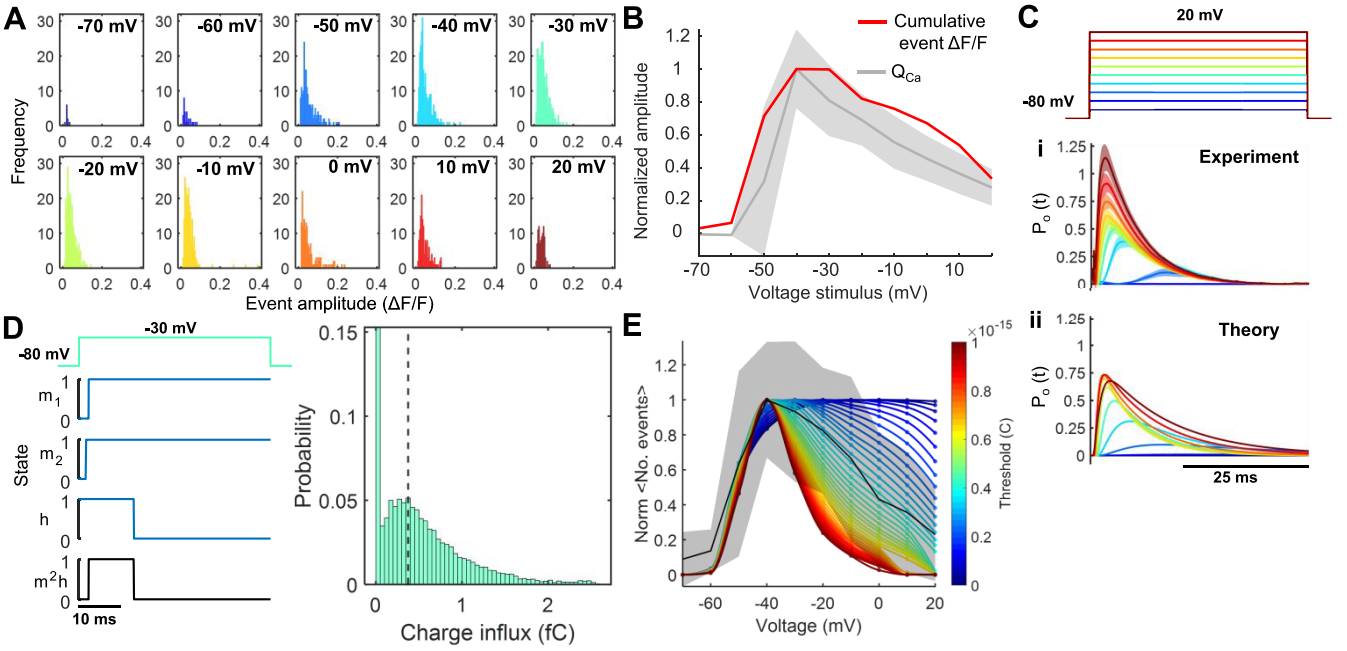

Figure 5. Single-molecule gating properties of $Ca_V3.2$. (A) Histograms of tether Ca^{2+} event amplitudes (10−277 events recorded per voltage stimulus, n = 25 tethers, 17 cells). (B) Cumulative amplitudes of the event histograms in (A) (red) and average charge influx for the corresponding cells (gray) as a function of voltage (n = 25 cell-tether pairs). Shading indicates std. dev. (C) $Ca_V3.2$ channel open probability, P_O, in response to depolarizing voltage steps from a holding potential of −80 mV (top). (i) P_O estimated from inward currents (n = 17 cells, shading indicates s.e.m.) and (ii) P_O calculated using a Hodgkin-Huxley-like model of gating transitions. (D) Left: stochastic simulation of a channel gating trajectory in response to depolarization of duration t_V. Blue traces show the individual gate trajectories, and black trace shows the channel state (m^2h). Right: distribution of charge influx, q, due to single-channel openings in response to depolarization to −30 mV for duration t_V ($n = 10^4$ channel trajectories). Calculated by integrating eq 7 in Note S2 over t_V. Black dashed line indicates predicted detection threshold from (E). (E) Frequency of observed events versus voltage (normalized, black, shading std. dev. of n = 19 tethers) and predicted single-channel event probability for different detection thresholds (colors). Color bar indicates simulated charge detection threshold (maximum R-value at 0.38 fC threshold). Using the average event frequency and thresholded event detection probability, we estimated the average linear density of channels to be ∼0.2 ± 0.1 μm^{-1} (mean ± s.d.; n = 16 tethers).

co-occurring within our detection window was ∼13%. We did not observe a correlation between the number of detected events and the tether radius.

Amplitude and Frequency of Single-Channel Gating Events. We next compared event characteristics reported by tether lck-jGCaMP8f to whole-cell electrical measures of channel gating. For each voltage step, we constructed a histogram of the unitary event amplitudes $(\Delta F/F)^t$ (Figure 5A). We reasoned that the ensemble average of these discrete gating events should reproduce the previously observed linear relationship between $(\Delta F/F)^t$ and (eq 5). To test this idea, we summed all unitary event amplitudes for each voltage. The plot of cumulative $(\Delta F/F)^t$ vs voltage closely followed the plot of Q^C_{Ca} vs voltage, determined from the whole-cell patch clamp measurements (Figure 5B). Thus, the fluorescence-detected Ca^{2+} events, when combined to create an ensemble average, recapitulated the voltage-dependent behavior of the macroscopic currents. This correspondence indicates that the gating properties of $Ca_V3.2$ were preserved upon channel partitioning into tethers.

We then sought to model the distribution of $(\Delta F/F)^t$ at each voltage. This distribution is not directly accessible from ensemble-average patch clamp measurements. We thus turned to stochastic simulations of channel gating. We fit a Hodgkin-Huxley-like model[36,37] of channel gating to the whole-cell currents recorded across voltage steps from −70 mV up to +20 mV (Figure 5C). We then performed stochastic simulations of single-channel gating, using the kinetic parameters derived from the fit to the whole-cell currents (Figure 5D and Table S2 and Notes S2 and S3 and Figure S7).[38,39] For each voltage step, we calculated the distribution of single-channel Q^t_{Ca} values, taking into account the voltage-dependent gating dynamics and the driving force for Ca^{2+} entry.

In the simulated single-channel trajectories, the probability of channel opening saturated at depolarized potentials (Figure S7). In contrast, we observed a decrease in the frequency of Ca^{2+} events at depolarized potentials (Figure 5E, black trace). At depolarized potentials, we expect faster $Ca_V3.2$ channel kinetics, lower driving force for Ca^{2+} entry and, thus, lower unitary charge passed by the channel. We hypothesized that these very small Ca^{2+} influx events might be below our detection threshold. To test this hypothesis, we applied a threshold to the simulated distributions of Q^t_{Ca} (Figure S7) and counted the voltage-dependent frequency of events that exceeded this threshold. Upon varying the simulated detection threshold, we found best correspondence between simulation and experiment at a threshold of 0.38 fC for jGCaMP8f and 0.4 fC for GCaMP6s (Figure 5D,E and Figure S8). This detection threshold corresponds to an equivalent constant current of ∼9 fA over t_V = 45 ms; or to 100 fA for a 4 ms gating event. These unitary charges are substantially smaller than are typically recorded by patch clamp.[6,7]

CONCLUSIONS

Historically, it has been challenging to measure small ionic or biomolecular fluxes in intact membranes. Here, we showed

https://doi.org/10.1021/acsnano.5c07589
ACS Nano XXXX, XXX, XXX−XXX

that membrane tethers can compartmentalize and thereby amplify single-channel fluxes. Using membrane-targeted GECIs in tethers, we detected puncta of elevated Ca^{2+} in response to voltage-dependent gating of a low-conductance $Ca_V3.2$ channel (Figure 4). Despite slow GECI kinetics, the tethers amplified and prolonged $[Ca^{2+}]$ transients enough that single-channel gating events were readily detectable (Figure 1).

We compared the amplitude and frequency of tether Ca^{2+} events to ensemble $Ca_V3.2$ electrophysiology. The mean height of tether Ca^{2+} transients correlated with the charge passed during depolarizing stimuli (Figures 3 and 5). Conversely, cell GECI fluorescence was poorly correlated with transported charge, likely due to intracellular Ca^{2+} transport. Pharmacological silencing of intracellular Ca^{2+} transport pathways might improve this correspondence. By comparing simulated single-channel gating trajectories and the observed frequency of Ca^{2+} events, we estimated a detection sensitivity of ~0.4 fC, corresponding to ~1250 Ca^{2+} ions (Figure 5). Strong buffering of intracellular Ca^{2+} presented a challenge for our measurements. It is estimated that the basal buffering capacity of cytoplasm ranges from 100 to 200,[27,29,40] so an influx of 1250 Ca^{2+} ions corresponds to only 6−13 free Ca^{2+} ions.

An extension of the current work would be to label the $Ca_V3.2$ channels directly, and to image their single-molecule fluorescence in a second fluorescence wavelength. This would provide an independent estimate of the number of channels in the tether. Additional fluorescence wavelengths could also be useful for independent fluorescent tags in the membrane or cytoplasm, either of which could be used to improve estimates of tether diameter.

In principle, our tether-based recording scheme can generalize to other proteins (e.g., channels, transporters, membrane associated enzymes). The key requirement is a suitable fluorescent reporter of the substrate or products.[10] For a 10 μm tether, a turnover rate of 100 s^{-1} at the distal end of the tether, and an unbuffered substrate with a diffusion coefficient of 200 $\mu m^2/s$, the local concentration increase is 1 μM, and the substrate residence time is 250 ms. These parameters benchmark the sensitivity needed for different substrate fluxes. Many parameters contribute to determining flux through a transport protein, including the chemical and electrical potentials of transported species, permeation mechanism, protein conformational dynamics, bilayer tension, post-translational modifications, cofactor binding, and redox chemistry.[1−3] Single-channel recordings in tethers open the door to exploring these factors in a cellular context.

We observed a good correspondence between the average $Ca_V3.2$ gating behavior in tethers and bulk $Ca_V3.2$ electrophysiology, which indicates that $Ca_V3.2$ channel gating is not disrupted in tethers. In general, however, isolation of proteins in tethers has the potential to perturb their function, e.g. via differences from the parent cell in membrane tension, curvature, or cytoskeletal and organellar associations.[21,41,42] As with any single-molecule technique, one must validate (e.g., by comparison to the ensemble-averaged bulk) that the isolation strategy does not perturb the molecule of interest.

Some cellular membranes natively contain nanoscale compartments, such as dendritic spines,[43] neurites,[44,45] primary cilia,[46] synaptic vesicles,[47] tunneling nanotubes,[48] and retraction fibers.[49] Our work highlights the possibility that stochastic single-channel gating events within these structures can lead to substantial fluctuations in substrate concentration. Whereas membrane signaling is typically modeled via ensemble-average kinetics, a direction for future research will be to explore the biological roles of stochastic single-molecule gating in nanoscale compartments.

METHODS

Genetic Constructs. We used membrane targeted lck-jGCaMP8f and GCaMP6s-CAAX Ca^{2+} indicators to detect single-channel tether Ca^{2+} transients. Both constructs were expressed under the control of a CMV promoter. The *pGP-CMV-GCaMP6s-CAAX* construct was a gift from Tobias Meyer (Addgene #52228) and used as provided. The *pGP-CMV-lck-jGCaMP8f* construct used in this work was made from a *pZac2.1-GfaABC1D-lck-jGCaMP8f* plasmid gifted by Loren Looger (Addgene #176759).

lck-jGCaMP8f was cloned into a pGP-CMV vector backbone (Addgene #104483) using Gibson assembly. Briefly, the vector was linearized by sequential digestion using restriction enzymes (New England Biolabs) and purified by GeneJET gel extraction kit (ThermoFisher). The insert fragment was generated by polymerase chain reaction amplification and inserted into the backbone using NEBuilder HiFi DNA assembly kit (New England Biolabs). The resulting construct was verified by sequencing (Primordium).

Cell Culture and Transfection. HEK293 cells stably expressing Tet repressor (T-REx-293, ThermoFisher), constitutive human $K_{ir}2.3$, and doxycycline-inducible human $Ca_V3.2$ were a generous gift from Terrance Snutch. $Ca_V3.2/K_{ir}2.3$ cells were maintained at 37 °C and 5% CO_2 in Dulbecco's modified Eagle's medium (DMEM) formulated with high glucose, GlutaMAX, and pyruvate (Cat. No. 10569010, ThermoFisher) and supplemented with 10% heat-inactivated fetal bovine serum, penicillin (100 U/mL), and streptomycin (100 μg/mL). Culture medium was supplemented with Geneticin (600 μg/mL, Life Technologies), hygromycin B (150 μg/mL, Sigma-Aldrich), and blasticidine (10 μg/mL, ThermoFisher) selection agents. Selection agents were removed and cells were passaged at least 24 h prior to transfection with GECI constructs. Passaged cells were grown to ~80% confluence prior to transfection with TransIT-293 (Mirus Bio) according to manufacturer protocols. $Ca_V3.2$ expression was induced 24−72 h prior to imaging using 150 pg/mL−15 ng/mL doxycycline (Sigma). A doxycycline dose of 1.5 ng/mL generated a whole cell $Ca_V3.2$ conductance of 5.6 ± 1.5 pS/μm^2 (n = 17 cells) at −20 mV (Figure S2E).

Patch-Clamp Electrophysiology. Whole cell voltage-clamp recordings were acquired from $Ca_V3.2$ expressing cells. On the morning of an experiment, cells were trypsinized and replated on poly-D-lysine (Sigma) coated glass bottom dishes (20 μg/mL incubated at RT overnight or 20 min at 37 °C, washed 3x with phosphate-buffered saline). Prior to an experiment, cells were washed 2x and immersed in an extracellular solution containing (in mM): 125 NaCl, 25 glucose, 15 HEPES, 2.5 KCl, 1 $MgCl_2$, 2 $CaCl_2$. Patch pipettes (1−10 MΩ) were filled with an internal solution containing (in mM): 8 NaCl, 130 $KMeSO_3$, 10 HEPES, 4 MgATP, 0.3 Na_3GTP, 5 KCl. The pH was adjusted to ~7.3 using KOH and the osmolarity was adjusted to ~295 mOsm/L with sucrose. Signals were amplified using an Axopatch 200B amplifier (Molecular Devices), filtered at 5 kHz and digitized at 100 kHz (DAQ PCIe-6323, National Instruments). A micromanipulator (Sutter) maneuvered patch pipettes to the cell membrane. Cell membrane voltage was clamped at a holding potential of −80 mV and then stimulated with depolarizing pulse trains (9× 45 ms pulses, 5 s interpulse rest, 15 s intertrain rest, Figure 2B,C). All experiments were performed at 32 °C with temperature control provided by an objective heater (Bioptechs) and stage heater (Warner).

Tether Formation. Micropipettes were pulled from glass capillaries (World Precision Instrument, 1B150F-4) using a pipette puller (Sutter P1000) and the tip of the pipette was sealed and rounded using a microforge (WPI, DMF1000) to form a microneedle. Microneedles were surface treated via incubation in poly-D-lysine (100 μg/mL, 37 °C for 20 min) followed by incubation in concanavalin A (100 μg/mL, Vector Laboratories) until use. A micromanipulator maneuvered the microneedle to the cell surface and

https://doi.org/10.1021/acsnano.5c07589
ACS Nano XXXX, XXX, XXX−XXX

tethers were formed upon brief contact and retraction of the microneedle tip from the membrane.

Imaging. Ca^{2+} imaging was performed on a custom-built inverted microscope using a 60x water immersion objective (Olympus, UPLSAPO60XW). Illumination, spatial light patterning, patch amplifier, data acquisition card, and camera were controlled with custom MATLAB (Mathworks) based software.[50] A digital micromirror device (DMD, Texas Instruments DLP3000) restricted 488 nm excitation light (81 mW/mm^2, PhoXX-488-60) to cell and tether ROIs. GECI fluorescence was imaged onto an EMCCD camera (DU-897E-CSO-#BV, Andor) with 300x electron-multiplying gain at a rate of 50−200 Hz. An adjustable slit (VA100, Thorlabs) restricted incident light to a subset of camera rows to enable high-speed imaging. Camera frames were either acquired at the rising edge of patch-clamp voltage stimuli or aligned in postprocessing. Fluorescence recordings were registered in time to the voltage-clamp data by reference to the shared the DAQ clock.

Image Processing and Ca^{2+} Event Finding. Tether orientation and transverse offset were identified using the Random Sample Consensus (RANSAC) algorithm.[51] Tether motion was compensated in postprocessing to stabilize the image of the tether. Fluorescence was averaged along the width (short axis) of the tether and plotted as a function of time and position along the length of the tether. To these kymographs, we applied a median filter and a spatiotemporal smoothing filter. We calculated a global threshold for each recording using Otsu's method.[52] To segment Ca^{2+} events, we thresholded each recording and assigned peak amplitude and position to local maxima.[53] Spontaneous Ca^{2+} activity typically appeared outside the narrow time window in which evoked events occurred. Stimulation epochs contaminated by spontaneous activity were thus identified and removed from our analysis. In instances where events were detected less than 0.7 μm apart, the smaller amplitude event was discarded. Additionally, we discarded any kymograph frames with greater than 0.5 events/μm.

Data Analysis. Data processing and image analysis were performed in MATLAB (Mathworks) and ImageJ.[54] Ca^{2+} diffusion modeling is described in Note S1. $Ca_V3.2$ channel modeling and stochastic simulations are described in Supplementary Notes S2 and S3. To compare observed Ca^{2+} event frequency to that predicted by our stochastic simulations (Figure 5D,E), we first calculated the mean events vs voltage per tether and then averaged across tethers. Then, starting with the simulated distributions of charge influx, we applied a charge detection threshold, and calculated the expected frequency of detected events vs voltage. We varied the simulated detection threshold to identify the threshold that gave closest correspondence to our data.

ASSOCIATED CONTENT

Supporting Information

The Supporting Information is available free of charge at https://pubs.acs.org/doi/10.1021/acsnano.5c07589.

Ensemble electrophysiology data for $Ca_V3.2$ expressed in HEK293 cells, whole-cell and single-channel fluorescence recordings of Ca^{2+} influx using GCaMP6s-CAAX, and descriptions of Ca^{2+} diffusion model, $Ca_V3.2$ gating model, and stochastic simulations (PDF)

AUTHOR INFORMATION

Corresponding Author

Adam E. Cohen − *Department of Chemistry and Chemical Biology and Department of Physics, Harvard University, Cambridge, Massachusetts 02138, United States;* orcid.org/0000-0002-8699-2404; Email: cohen@chemistry.harvard.edu

Author

Madeleine R. Howell − *Department of Chemistry and Chemical Biology, Harvard University, Cambridge, Massachusetts 02138, United States;* orcid.org/0009-0005-4263-5279

Complete contact information is available at: https://pubs.acs.org/10.1021/acsnano.5c07589

Notes

An initial version of this manuscript was submitted to a preprint server: Howell, Madeleine R.; Cohen, Adam E. Optical single-channel recording via diffusional confinement in membrane tethers. 2025, 652649. bioRxiv. 10.1101/2025.05.07.652649 (accessed June 26, 2025).

The authors declare no competing financial interest.

ACKNOWLEDGMENTS

We thank A. Preecha, S. Begum, and C. Bodden for technical assistance, S. Innes-Gold, H. Davis, and F.P. Brooks for assistance with instrumentation, P. Park and Y. Wang for assistance with electrophysiology, and E. Moult and K. Xiang for helpful discussions regarding data analysis and modeling. We thank T. Meyer, L. Looger, and D. Kim for GECI plasmid constructs and T. Snutch for the $Ca_V3.2$ cell line. This work was supported by Vannevar Bush Faculty Fellowship N00014-18-1-2859 (A.E.C.), NSF Quantum Sensing for Biophysics and Bioengineering (QuBBe) Quantum Leap Challenge Institute (QLCI) grant OMA-2121044, and National Science Foundation Graduate Research Fellowship Grant #DGE 2140743 (M.R.H.). Figure 1 and Figures S1C and S2A and TOC graphic contain elements created in BioRender (Howell, M. (2025) https://BioRender.com/r68vq1t).

REFERENCES

(1) Modak, A.; Kilic, Z.; Chattrakun, K.; Terry, D. S.; Kalathur, R. C.; Blanchard, S. C. Single-Molecule Imaging of Integral Membrane Protein Dynamics and Function. *Annu. Rev. Biophys.* **2024**, *53* (1), 427−453.

(2) Hediger, M. A.; Clémençon, B.; Burrier, R. E.; Bruford, E. A. The ABCs of Membrane Transporters in Health and Disease (SLC Series): Introduction. *Mol. Aspects Med.* **2013**, *34* (2), 95−107.

(3) Hille, B. *Ion Channels of Excitable Membranes*; Sinauer: Sunderland, MA, 2001; Vol. *507*.

(4) Neher, E.; Sakmann, B. Single-Channel Currents Recorded from Membrane of Denervated Frog Muscle Fibres. *Nature* **1976**, *260* (5554), 799−802.

(5) Hamill, O. P.; McBride, D. W. Rapid Adaptation of Single Mechanosensitive Channels in Xenopus Oocytes. *Proc. Natl. Acad. Sci. U. S. A.* **1992**, *89* (16), 7462−7466.

(6) Plested, A. J. R. Single-Channel Recording of Ligand-Gated Ion Channels. *Cold Spring Harbor Protoc.* **2016**, *2016* (8), No. pdb-top087239.

(7) Hamill, O. P.; Marty, A.; Neher, E.; Sakmann, B.; Sigworth, F. J. Improved Patch-Clamp Techniques for High-Resolution Current Recording from Cells and Cell-Free Membrane Patches. *Pflügers Archiv Eur. J. Physiol.* **1981**, *391* (2), 85−100.

(8) Levis, R. A.; Rae, J. L. The Use of Quartz Patch Pipettes for Low Noise Single Channel Recording. *Biophys. J.* **1993**, *65* (4), 1666−1677.

(9) Scheppach, C.; Robinson, H. P. C. Fluctuation Analysis in Nonstationary Conditions: Single Ca^{2+} Channel Current in Pyramidal Neurons. *Biophys. J.* **2017**, *113* (11), 2383−2395.

(10) Greenwald, E. C.; Mehta, S.; Zhang, J. Genetically Encoded Fluorescent Biosensors Illuminate the Spatiotemporal Regulation of Signaling Networks. *Chem. Rev.* **2018**, *118* (24), 11707−11794.

(11) Wang, S.-Q.; Song, L.-S.; Lakatta, E. G.; Cheng, H. Ca^{2+} Signalling between Single L-Type Ca^{2+} Channels and Ryanodine Receptors in Heart Cells. *Nature* **2001**, *410* (6828), 592−596.
(12) Demuro, A.; Parker, I. Optical Single-Channel Recording: Imaging Ca^{2+} Flux through Individual N-Type Voltage-Gated Channels Expressed in *Xenopus* Oocytes. *Cell Calcium* **2003**, *34* (6), 499−509.
(13) Demuro, A.; Parker, I. "Optical Patch-Clamping": Single-Channel Recording by Imaging Ca^{2+} Flux through Individual Muscle Acetylcholine Receptor Channels. *J. Gen. Physiol.* **2005**, *126* (3), 179−192.
(14) Smith, I. F.; Parker, I. Imaging the Quantal Substructure of Single IP3R Channel Activity during Ca^{2+} Puffs in Intact Mammalian Cells. *Proc. Natl. Acad. Sci. U. S. A.* **2009**, *106* (15), 6404−6409.
(15) Zou, H.; Lifshitz, L. M.; Tuft, R. A.; Fogarty, K. E.; Singer, J. J. Visualization of Ca^{2+} Entry through Single Stretch-Activated Cation Channels. *Proc. Natl. Acad. Sci. U. S. A.* **2002**, *99* (9), 6404−6409.
(16) Dynes, J. L.; Amcheslavsky, A.; Cahalan, M. D. Genetically Targeted Single-Channel Optical Recording Reveals Multiple Orai1 Gating States and Oscillations in Calcium Influx. *Proc. Natl. Acad. Sci. U. S. A.* **2016**, *113* (2), 440−445.
(17) Sanchez, C.; Berthier, C.; Tourneur, Y.; Monteiro, L.; Allard, B.; Csernoch, L.; Jacquemond, V. Detection of Ca^{2+} Transients near Ryanodine Receptors by Targeting Fluorescent Ca^{2+} Sensors to the Triad. *J. Gen. Physiol.* **2021**, *153* (4), No. e202012592.
(18) Bertaccini, G. A.; Casanellas, I.; Evans, E. L.; Nourse, J. L.; Dickinson, G. D.; Liu, G.; Seal, S.; Ly, A. T.; Holt, J. R.; Wijerathne, T. D.; Yan, S.; Hui, E. E.; Lacroix, J. J.; Panicker, M. M.; Upadhyayula, S.; Parker, I.; Pathak, M. M. Visualizing PIEZO1 Localization and Activity in hiPSC-Derived Single Cells and Organoids with HaloTag Technology. *bioRxiv* **2023**, No. 573117.
(19) Fitzgerald, G. A.; Terry, D. S.; Warren, A. L.; Quick, M.; Javitch, J. A.; Blanchard, S. C. Quantifying Secondary Transport at Single-Molecule Resolution. *Nature* **2019**, *575* (7783), 528−534.
(20) Ciftci, D.; Huysmans, G. H. M.; Wang, X.; He, C.; Terry, D.; Zhou, Z.; Fitzgerald, G.; Blanchard, S. C.; Boudker, O. Single-Molecule Transport Kinetics of a Glutamate Transporter Homolog Shows Static Disorder. *Sci. Adv.* **2020**, *6* (22), No. eaaz1949.
(21) Shi, Z.; Graber, Z. T.; Baumgart, T.; Stone, H. A.; Cohen, A. E. Cell Membranes Resist Flow. *Cell* **2018**, *175* (7), 1769−1779.e13.
(22) Perez-Reyes, E. Molecular Physiology of Low-Voltage-Activated T-Type Calcium Channels. *Physiol. Rev.* **2003**, *83* (1), 117−161.
(23) Weber, A. M.; Wong, F. K.; Tufford, A. R.; Schlichter, L. C.; Matveev, V.; Stanley, E. F. N-Type Ca^{2+} Channels Carry the Largest Current: Implications for Nanodomains and Transmitter Release. *Nat. Neurosci.* **2010**, *13* (11), 1348−1350.
(24) Chen, T.-W.; Wardill, T. J.; Sun, Y.; Pulver, S. R.; Renninger, S. L.; Baohan, A.; Schreiter, E. R.; Kerr, R. A.; Orger, M. B.; Jayaraman, V.; Looger, L. L.; Svoboda, K.; Kim, D. S. Ultrasensitive Fluorescent Proteins for Imaging Neuronal Activity. *Nature* **2013**, *499* (7458), 295−300.
(25) Zhang, Y.; Rózsa, M.; Liang, Y.; Bushey, D.; Wei, Z.; Zheng, J.; Reep, D.; Broussard, G. J.; Tsang, A.; Tsegaye, G.; Narayan, S.; Obara, C. J.; Lim, J.-X.; Patel, R.; Zhang, R.; Ahrens, M. B.; Turner, G. C.; Wang, S. S.-H.; Korff, W. L.; Schreiter, E. R.; Svoboda, K.; Hasseman, J. P.; Kolb, I.; Looger, L. L. Fast and Sensitive GCaMP Calcium Indicators for Imaging Neural Populations. *Nature* **2023**, *615* (7954), 884−891.
(26) Murthy, V. N.; Sejnowski, T. J.; Stevens, C. F. Dynamics of Dendritic Calcium Transients Evoked by Quantal Release at Excitatory Hippocampal Synapses. *Proc. Natl. Acad. Sci. U. S. A.* **2000**, *97* (2), 901−906.
(27) Dupont, G.; Falcke, M.; Kirk, V.; Sneyd, J. *Models of Calcium Signalling*; Interdisciplinary Applied Mathematics; Springer International Publishing: Cham, 2016; Vol. *43* .
(28) Allbritton, N. L.; Meyer, T.; Stryer, L. Range of Messenger Action of Calcium Ion and Inositol 1,4,5-Trisphosphate. *Science* **1992**, *258* (5089), 1812−1815.
(29) Higley, M. J.; Sabatini, B. L. Calcium Signaling in Dendrites and Spines: Practical and Functional Considerations. *Neuron* **2008**, *59* (6), 902−913.
(30) Shuai, J.; Parker, I. Optical Single-Channel Recording by Imaging Ca^{2+} Flux through Individual Ion Channels: Theoretical Considerations and Limits to Resolution. *Cell Calcium* **2005**, *37* (4), 283−299.
(31) Derényi, I.; Jülicher, F.; Prost, J. Formation and Interaction of Membrane Tubes. *Phys. Rev. Lett.* **2002**, *88* (23), No. 238101.
(32) Naraghi, M.; Neher, E. Linearized Buffered Ca^{2+} Diffusion in Microdomains and Its Implications for Calculation of $[Ca^{2+}]$ at the Mouth of a Calcium Channel. *J. Neurosci.* **1997**, *17* (18), 6961−6973.
(33) Sabatini, B. L.; Maravall, M.; Svoboda, K. Ca^{2+} Signaling in Dendritic Spines. *Curr. Opin. Neurobiol.* **2001**, *11* (3), 349−356.
(34) Belardetti, F.; Tringham, E.; Eduljee, C.; Jiang, X.; Dong, H.; Hendricson, A.; Shimizu, Y.; Janke, D. L.; Parker, D.; Mezeyova, J.; Khawaja, A.; Pajouhesh, H.; Fraser, R. A.; Arneric, S. P.; Snutch, T. P. A Fluorescence-Based High-Throughput Screening Assay for the Identification of T-Type Calcium Channel Blockers. *ASSAY Drug Dev. Technol.* **2009**, *7* (3), 266−280.
(35) Spruston, N.; Jaffe, D. B.; Williams, S. H.; Johnston, D. Voltage- and Space-Clamp Errors Associated with the Measurement of Electrotonically Remote Synaptic Events. *J. Neurophysiol.* **1993**, *70* (2), 781−802.
(36) Huguenard, J. R.; McCormick, D. A. Simulation of the Currents Involved in Rhythmic Oscillations in Thalamic Relay Neurons. *J. Neurophysiol.* **1992**, *68* (4), 1373−1383.
(37) Destexhe, A.; Huguenard, J. R. Nonlinear Thermodynamic Models of Voltage-Dependent Currents. *J. Comput. Neurosci.* **2000**, *9* (3), 259−270.
(38) Thompson, S. M. Relations between Chord and Slope Conductances and Equivalent Electromotive Forces. *Am. J. Physiol.-Cell Physiol.* **1986**, *250* (2), C333−C339.
(39) Gillespie, D. T. Exact Stochastic Simulation of Coupled Chemical Reactions. *J. Phys. Chem.* **1977**, *81* (25), 2340−2361.
(40) Eisner, D.; Neher, E.; Taschenberger, H.; Smith, G. Physiology of Intracellular Calcium Buffering. *Physiol. Rev.* **2023**, *103* (4), 2767−2845.
(41) Yang, S.; Miao, X.; Arnold, S.; Li, B.; Ly, A. T.; Wang, H.; Wang, M.; Guo, X.; Pathak, M. M.; Zhao, W.; Cox, C. D.; Shi, Z. Membrane Curvature Governs the Distribution of Piezo1 in Live Cells. *Nat. Commun.* **2022**, *13* (1), 7467.
(42) Domanov, Y. A.; Aimon, S.; Toombes, G. E. S.; Renner, M.; Quemeneur, F.; Triller, A.; Turner, M. S.; Bassereau, P. Mobility in Geometrically Confined Membranes. *Proc. Natl. Acad. Sci. U. S. A.* **2011**, *108* (31), 12605−12610.
(43) Sabatini, B. L.; Svoboda, K. Analysis of Calcium Channels in Single Spines Using Optical Fluctuation Analysis. *Nature* **2000**, *408* (6812), 589−593.
(44) Xiang, K. M.; Park, P.; Koren, S. A.; Hayward, R. F.; Cohen, A. E. All-Optical Mapping of cAMP Transport Reveals Rules of Sub-Cellular Localization. *bioRxiv* **2023**, No. 546633.
(45) Hayward, R. F.; Cohen, A. E. All-Optical Mapping of Ca^{2+} Transport and Homeostasis in Dendrites. *Cell Calcium* **2025**, *125*, No. 102983.
(46) Truong, M. E.; Bilekova, S.; Choksi, S. P.; Li, W.; Bugaj, L. J.; Xu, K.; Reiter, J. F. Vertebrate Cells Differentially Interpret Ciliary and Extraciliary cAMP. *Cell* **2021**, *184* (11), 2911−2926.e18.
(47) Mutch, S. A.; Kensel-Hammes, P.; Gadd, J. C.; Fujimoto, B. S.; Allen, R. W.; Schiro, P. G.; Lorenz, R. M.; Kuyper, C. L.; Kuo, J. S.; Bajjalieh, S. M.; Chiu, D. T. Protein Quantification at the Single Vesicle Level Reveals That a Subset of Synaptic Vesicle Proteins Are Trafficked with High Precision. *J. Neurosci.* **2011**, *31* (4), 1461−1470.
(48) Smith, I. F.; Shuai, J.; Parker, I. Active Generation and Propagation of Ca^{2+} Signals within Tunneling Membrane Nanotubes. *Biophys. J.* **2011**, *100* (8), L37−L39.
(49) Dharan, R.; Huang, Y.; Cheppali, S. K.; Goren, S.; Shendrik, P.; Wang, W.; Qiao, J.; Kozlov, M. M.; Yu, L.; Sorkin, R. Tetraspanin 4

https://doi.org/10.1021/acsnano.5c07589
ACS Nano XXXX, XXX, XXX−XXX

Stabilizes Membrane Swellings and Facilitates Their Maturation into Migrasomes. *Nat. Commun.* **2023**, *14* (1), 1037.
(50) Itkis, D. G.; Brooks, F. P.; Davis, H. C.; Hotter, R.; Wong-Campos, J. D.; Qi, Y.; Jia, B. Z.; Howell, M.; Xiong, M.; Hayward, R. F.; Lee, B. H.; Wang, Y.; Perelman, R. T.; Cohen, A. E. Luminos: Open-Source Software for Bidirectional Microscopy. *bioRxiv* **2025**, No. 639658.
(51) Torr, P. H. S.; Zisserman, A. MLESAC: A New Robust Estimator with Application to Estimating Image Geometry. *Comput. Vis. Image Underst.* **2000**, *78* (1), 138−156.
(52) Otsu, N. A Threshold Selection Method from Gray-Level Histograms. *IEEE Trans. Syst. Man Cybern.* **1979**, *9* (1), 62−66.
(53) Natan, A. *Fast 2D peak finder* https://www.mathworks.com/matlabcentral/fileexchange/37388-fast-2d-peak-finder 2021 (accessed 2025−03−28).
(54) Schneider, C. A.; Rasband, W. S.; Eliceiri, K. W. NIH Image to ImageJ: 25 Years of Image Analysis. *Nat. Methods* **2012**, *9* (7), 671−675.

https://doi.org/10.1021/acsnano.5c07589
ACS Nano XXXX, XXX, XXX−XXX